Assessment of W density in LHD core plasmas using visible forbidden lines of highly charged W ions

Daiji Kato[1,2], Hiroyuki A. Sakaue[1], Izumi Murakami[1,3], Motoshi Goto[1,3], Tetsutaro Oishi[1,3], Naoki Tamura[1,3], Hisamichi Funaba[1,3] and Shigeru Morita[1,3]

[1] National Institute for Fusion Science, 322-6 Oroshi-cho, Toki, Gifu 509-5292, Japan
[2] Interdisciplinary Graduate School of Engineering and Sciences, Kyushu University, Kasuga, Fukuoka 816-8580, Japan
[3] Department of Fusion Science, The Graduate University for Advanced Studies, SOKENDAI, 322-6 Oroshi-cho, Toki, Gifu 509-5292, Japan

E-mail: kato.daiji@nifs.ac.jp

Received xxxxxx
Accepted for publication xxxxxx
Published xxxxxx

Abstract

Visible magnetic-dipole (M1) lines can serve as a novel diagnostic mean of tungsten in ITER and future DEMO reactors. Here a local tungsten density in core plasmas of the Large Helical Device (LHD) is successfully assessed with the measurement of visible M1 lines emitted by W^{26+} and W^{27+}. By such a measurement, (i) the radial profile of total tungsten density in the LHD core plasmas with a line-averaged electron density of ~ 4×10^{19} m^{-3} and central electron temperature of ~ 1 keV is found to be a hollow, and (ii) the total tungsten density is found to be decreased in the whole region with an increase in the electron temperature due to the onset of reheat mode. The scheme with visible M1 lines used in the present work can be also applied for the tungsten density measurement at the ITER edge plasma.

Keywords: Tungsten, LHD, Visible spectroscopy, ITER

1. Introduction

Tungsten transport and its density control in plasmas are key issues in order to maintain high-performance plasmas in ITER with a tungsten divertor because it is well known that a tungsten has a strong radiation cooling power. Electron temperature in ITER can range from 0.1 keV at the edge up to about 20 keV at the plasma center. In such a plasma, tungsten can be highly ionized (q = 20 - 60) and can emit strong line emissions in extreme-ultraviolet (EUV) and soft X-ray regions. Pütterich et al. [1] investigated the tungsten transport in the core plasma of JET by deriving tungsten concentration profiles from signals of soft X-ray cameras. In type-I ELMy H-modes with neutral beam heating, they found tungsten accumulation in the core $\rho < 0.3$ approaching tungsten concentration of 10^{-3} in between sawtooth crashes. The tungsten accumulation causes strong radiation at the plasma centre and flattening of the electron temperature profile. The flattening of the temperature profile reduces turbulent transport and effects of turbulent outward pinch. The neoclassical inward drift causes further accumulation of tungsten [2]. On the other hand, central ion cyclotron heating (ICRH) could remove tungsten from the core, while the electron temperature increased and the density profile became less peaked. The surpression of tungsten accumulation was observed also in Alcator C-Mod H-mode plasmas [3] with

ICRH heating only. In long pulse WEST L-mode plasmas, it was reported that turblent transport manifesting at high ratios of electron temperatures to ion temperatures (T_e/T_i) mitigated tungsten accumulation [4]. Although such driving mechanisms have been identified with tokamak machines, tungsten transport is still hard to predict mainly due to the fact that subtle change in plasma profiles result in significant effects on the tungsten transport. Comprehensive understanding required for predicting effects of MHD mode activity, turbulent transport, and neoclassical transport are yet to be obtained. From a view point of atomic processes, the tungsten transport simulation has a peculiar difficulty because many charge states whose ionization and recombination rate coefficients still have large uncertainties are involved.

Calculations of cooling factors of tungsten have been improved with the aid of a detailed atomic model [5,6]. Recombination rate coefficients of the model are adjusted to reconcile calculated relative ion abundances with bolometric and spectroscopic measurements of radiation from tungsten accumulated in the central part of core plasmas at ASDEX Upgrade [7]. Murakami et al. performed calculations of the cooling factors adopting relative ion abundances determined by matching synthesized EUV line spectra of tungsten highly charged ions to measured line spectra at LHD [8]. These calculations are approximately consistent. However, direct measurements of the cooling factors [5, 9] have a large uncertainty as independent measurements of total tungsten density in plasmas are inaccurate. In other words, reliable independent measurements of the total tungsten density are highly relevant to accurate evaluation of the cooling factors.

Until now, only a few direct measurements of the tungsten density with spectroscopic diagnostics have been reported for emission lines in the EUV range [10]. Kato et al. reported observation of visible lines emitted from highly charged tungsten ions due to magnetic-dipole (M1) transitions in the LHD core plasmas after a tungsten pellet injection [11]. Such visible M1 lines are useful particularly for fusion plasmas because mirrors and optical fibers can be used for avoiding a direct neutron radiation on detectors. Currently, the W^{26+} ion density can be also assessed by using the measurement of two M1 lines (335.7 nm and 333.7 nm), in addition to the W^{27+} ion density assessed by the measurement of a M1 line (337.7 nm) [12], and then a total tungsten density in the LHD core plasmas can be assessed based on such ion densities.

In section 2, an LHD discharge for the tungsten pellet injection experiment and measurements of visible M1 lines of W^{26+} and W^{27+} are explained. In section 3, vertical profiles of the M1 line intensities on a poloidal cross section are presented. Methods to derive tungsten densities from the vertical profiles are also described with detailed atomic processes relevant to the M1 line emission. In section 4, derived ion densities of W^{26+} and W^{27+} are presented, and the ion density ratios are examined by a tungsten transport simulation. Based on these results, total tungsten densities in the core plasma are presented and discussed before summary.

2. Tungsten pellet injection and visible spectroscopy at LHD

Figure 1 shows time traces for the discharge of interest. In this discharge, a polyethylene tube containing a tungsten wire (0.6 mm long and 0.15 mm diameter, i.e., the number of tungsten particle is about 6.8×10^{17}/pellet) [12] is injected at the time of 4.03 s. After the tungsten injection, the central electron temperature, T_e, decreases to $\sim$1 keV due to the strong radiation by the tungsten ions. Then, the central electron temperature remains at an almost constant value until t = 5.4 s, while the line-averaged electron density gradually increases due to a hydrogen gas puff. About 0.1 s after the hydrogen gas puff is stopped at t = 5.3 s, the electron temperature is increased, meanwhile the line-averaged electron density is decreased. Such changes in electron temperature and density can be considered due to the onset of a reheat mode [13].

The pellet is accelerated by pressurized He gas of 10 – 20 atm and injected with the angle of 12˚ tilted from the normal to the toroidal magnetic axis [14]. Time-resolved (exposure time for 38 ms at every 100 ms) measurements of emission spectra were performed using a Czerny-Turner visible-UV spectrometer (slit width of 50 μm and grating of 1200 gr/mm) equipped with a CCD detector [15]. Absolute intensity calibration of the spectrometer was performed with an integrating sphere using the same optical system as the actual measurement. Figure 2 shows an observation port as well as the pellet injection port. Photon emission is detected through optical fibers at 44 lines of sight along the vertical direction (Z) of a horizontally elongated poloidal cross section, as shown in Fig. 2. The poloidal cross section is asymmetric with respect to Z = 0 because the cross section is 6˚ tilted from the normal to the toroidal magnetic axis.

Figures 3 shows a time trace of photon detection counts in 330 - 340 nm for t = 3.8 – 6.0 s in the discharge. Wavelength calibration was done using emission lines of hydrogen and helium in the same discharges. Uncertainties in the wavelength calibration are estimated to be about 0.02 nm. Emission lines indicated by arrows are absent in the spectrum before the tungsten pellet injection. These lines are assigned to the emission lines from tungsten. Figure 4 shows vertical distributions of these emission lines (upper panel) and the spectrum (lower panel) at t = 4.1 s. The tungsten lines have large intensities inside the vertical edge of the core plasma (Z < 0.4 m), while other intrinsic lines (e.g. O IV lines) have broader vertical distributions of the intensities. The lines at 333.7 nm and 335.7 nm are identified as the M1 lines of W^{26+} in the ground state ($4f^2$) $^3F_4 \rightarrow {}^3F_3$ and $^3F_4 \rightarrow {}^1G_4$, respectively [16]. It is noted that these two M1 lines share the common

upper level. The line at 337.7 nm is identified as the M1 line of W^{27+} in the ground state (4f) $^2F_{7/2} \rightarrow {}^2F_{5/2}$ [17]. In Table 1, wavelengths and transitions of these M1 lines are listed and compared with previous electron-beam-ion-trap (EBIT) measurements [16-20] and theoretical calculations [16,17,20-22]. The present measurements are in good agreement with the EBIT measurements. Uncertainty of the experimental values is less than that of the theoretical values. The experimental wavelengths, therefore, serve as a benchmark for accuracy of the theoretical calculations. Another three lines observed at 332.0 nm, 334.2 nm, and 334.5 nm are also presumably assigned to tungsten in different charge states, although the charge states and transitions are yet to be identified.

3. Vertical profile of M1 line intensity and methods of analysis

The vertical profiles of the M1 lines of W^{26+} and W^{27+} for t = 4.1 – 5.6 s are shown in Fig. 5. The vertical profile at t = 4.1 s when the central electron temperature $T_e(0) \sim 2$ keV is hollow having a dip around Z = 0, while the profiles become peaked at Z = 0 in later times when $T_e(0) \sim 1$ keV. These vertical profiles, $I_{ij}(Z)$, can be related to the density of W^{q+} ions, n_{Wq+}, emitting photons by the transition $j \rightarrow i$ as,

$$I_{ij}(Z) = A_{ij} \int n_j^{(q)} n_{Wq+} dX, \tag{1}$$

where A_{ij} is a transition rate and $n_j^{(q)}$ a fractional population of the upper level. In Table 2, M1 transition rates of the lines of interest calculated independently with HULLAC [23], FAC [24], and GRASP2K [25] codes are compared. The HULLAC and FAC codes are based on parametric potential method whereas the GRASP2K code based on the multi-configurational Dirack-Hatree-Fock method for calculations of electronic wave functions. All of the independent calculations give consistent results. Unsertainty in the theoretical transition rates is less than 10 %. Electric-quadruple (E2) transition rates for these transitions were calculated to be negligibly smaller than the M1 transition rates. No experimental rate is available for these forbidden transitions. In the following analysis, the transition rates of HULLAC code are adopted.

The fractional population of the upper level, which depends on local electron temperature T_e and density n_e, is calculated by a collisional-radiative model adopting T_e and n_e measured by Thomson scattering,

$$\left[\sum_{j\neq i}\left(n_e C_{ji}^e + n_p C_{ji}^p\right) + n_e S_i^{q\rightarrow q+1} + \sum_{j<i} A_{ji}\right] n_i^{(q)} = \sum_{j\neq i}\left(n_e C_{ij}^e + n_p C_{ij}^p\right) n_j^{(q)} + \sum_{j>i} A_{ij} n_j^{(q)}, \tag{3}$$

where n_e and n_p are electron and proton densities, respectively, C_{ij}^e and C_{ij}^p (de-)excitation rate coefficients by electron and proton collisions, respectively, $S_i^{q\rightarrow q+1}$ ionization rate coefficients by electron collisions. The collisional rate coefficients were calculated from cross sections assuming the Maxwellian velocity distribution of electrons and protons. The energy levels, the radiative transition rates (E1, E2, E3, M1, and M2) and electron distorted-wave cross sections were calculated using HULLAC code [23]. Cross sections of proton collisions were calculated in a semi-classical perturbation approximation [12]. In the present calculations, the electric-quadruple interaction between protons and tungsten ions is taken into account, and $T_p = T_e$ and $n_p = n_e$ are assumed. The assumption of $T_p = T_e$ is probably valid at the high electron densities $n_e > 3.0 \times 10^{19}$ m^{-3} of the present discharge.

Figure 6 shows schematic diagrams of primary population flows for the M1 line emissions of W^{26+} and W^{27+}. As shown in the figure, the upper level populations for both are mainly provided via the radiative decays from the $4d^9 4f^3$ and $4d^9 4f^2$ excited states, respectively. Such 4d – 4f transitions make the strong line emission in the extreme-ultraviolet (EUV) region of 5 – 6 nm [26-29]. The proton collisions make transitions of metastable levels in the excited states to the levels allowed for the electric-dipole transition to the ground state. As a result, the fractional population of the upper level is increased by 40 % for the W^{27+} (4f) M1 line. The same is anticipated for $4d^9 4f^3$ states of W^{26+} ions. However, such proton collision effects give only a few % increase in the upper level fractional population for the two W^{26+} ($4f^2$) M1 lines. Product of the transition rate and the fractional population of the upper level devided by the local n_e, i.e. $\varepsilon_{ij} = A_{ij} \times n_j^{(q)}/n_e$, is called as photon emission coefficient (PEC). Figure 7 shows local T_e and n_e measured by Thomson scattering as a function the normalized minor radius for t = 5.0 s of the present discharge and corresponding PECs. The PECs show a uniform radial profile except at the edge region where the n_e decreases significantly. The PECs of the M1 lines increase as the local n_e decreases because due to small radiative transition rates fractional populations of the upper levels are effectively decreased by collisions at higer densities. Enhancement of the PECs by the proton collision becomes significant at temperatures above about 300 eV as seen in the figure.

In the pesent analysis, poloidally symmetric distributions for the tungsten ions in the core are assumed. Such radial distribution of n_{Wq+} is represented by a Gaussian basis set centered at each normalized minor radius ρ_k $(k = 1, \cdots, N)$ as

$$n_{Wq+} = \frac{1}{\sqrt{2\pi\sigma^2}} \sum_{k=1}^{N} \exp[-(\rho - \rho_k)^2/(2\sigma^2)]\, b_k.$$

(2)

A set of the coefficients $\{b_k\}$ were determined by minimizing squared redisuals of Eq. (1) and the measured vertical profiles taking the geometry of the poloidal cross section into account (see Fig. 8). It is noted that the T_e and n_e values for the PECs are averaged for the sampling time of the spectroscopic measurements (38 ms), and its radial profiles are smoothened by polynomial interlolations. The σ^2 parameter is set arbitrarily, which represents correlation between the coefficients of adjacent radial sectors and effectively supresses scattering in the radial distribution of n_{Wq+}. The vertical profiles reconstracted with so-obtained n_{W26+} and n_{W27+} with $\sigma = 0.12/a_{99}$ are shown by solid curves in Fig. 5.

4. Assessment of tungsten density

The radial distributions of n_{W26+} and n_{W27+} obtained in the present work are shown in Fig. 9. Temporal behavior of each ion density is entangled with those of total tungsten density, n_W, and each fractional ion abundance of W^{q+}, n_q, as $n_{Wq+} = n_W \times n_q$. Influence of n_W is cancelled in the ion density ratios, $n_{Wq+}/n_{Wq'+} = n_q/n_{q'}$. Such ion density ratios of n_{27}/n_{26} are ploted in Fig. 10. The results are fairly in good agreement with the ratios of the ionization equilibrium model, which were calculated adopting ionization and recombination rate coefficients of Atomic Data and Analysis Structure (ADAS) database [30] and local T_e and n_e measured by Thomson scattering, except for radial regions where the ion densities are vanishingly small. The agreement seems to be better for the ratios obtained taking the proton collision effects into account.

In order to examine validity of the ionization equilibrium hypothesis, we performed tungsten transport simulation with STRAHL code [31] using the same ionization and recombination rate coefficients of the ADAS database. The code solves the radial continuity equation for each ionization stage of tungsten in 1-D geometry using the T_e and n_e radial profiles measured by Thomson scattering. Present radial transport model assumes a uniform diffusion coefficient of 0.1 m^2/s and inward drift velocities in the edge region (linear interpolation of 0.0, -2.0, -1.0, and 0.0 m/s at $\rho = 1.0, 0.9, 0.7,$ and 0.5, respectively, and 0.0 m/s for $\rho < 0.5$) as dipicted in Fig. 11. These transport coefficients are set the same values for every charge state and constant over time during the simulation. A neutral tungsten source of 6.8×10^{17} W ramping up in 6 ms at the edge is given to represent the pellet ablation. Figure 12 shows distributions of fractional W^{q+} abundance at $\rho = 0.0$ and 0.8 for t = 5.0 s and 5.6 s obtained by the transport-free ionization equilibrium model and the transport simulation. Both results agree very well indicating validity of the transport-free ionization equilibrium model. Discrepancy due to non-equilibrium ionization induced by transport is seen only for lower charge states at t = 5.0 s whose fractional abundance is negligibly small. The same observation was reported at ASDEX Upgrade [7] in evaluation of effects of the neoclassical inward drift on fractional ion abundances of tungsten inside the accumulation region. A minor effect on the equilibrium was only visible for transport coefficients much larger than predicted for the neoclassical inward drift.

Based on the above result, total tungsten densities are obtained from the W^{27+} ion densities dividing by the theoretical fractional ion abundances of the ionization equilibrium model. Figure 13 shows time evolution of the total tungsten densities for t = 4.8 – 5.6 s. In the Fig. 14, corresponding electron temperature profiles of the present measuerments are plotted. Until t = 5.4 s, the electron temperatures in the central region ($\rho < 0.4$) are almost constant, while a shoulder of the temperature profile is developed in $\rho = 0.4 - 0.8$. At t = 4.8 s, a steep temperature gradient is also observed in $\rho = 0.6 - 0.7$ which becomes less significant as the shoulder at the edge developes. It may be noteworthy that an abrupt drop of the tungsten density in $\rho = 0.6 - 0.7$ only apparent at t = 4.8 s is significant. The total tungsten densities are gradually decreasing with time, while the densities in $\rho = 0.3 - 0.4$ are almost constant leading to a hollow profile of the radial distribution at t = 5.4 s. After the onset of reheat mode (from t = 5.4 s), in which the core electron temperature increases significantly (see the electron temperatures at t = 5.6 s in Fig. 14), a rapid reduction of the total tungsten density is observed in the whole radial region. This reduction coincides apparently with decrease in the bolometric radiation power (see Fig. 1). It is difficult to explain such rapid reduction of the total tungsten density during the reheat mode by the constant transport coefficients. It may therefore be suggested that the radial transport of tungsten is enhanced in the reheat mode and the elevated electron temperature play a role. Nevertheless, mechanisms of such enhanced transport in the reheat mode are yet to be understood.

It is difficult to reconcile the present total tungsten density with the number of tungsten atoms contained in the pellet (6.8×10^{17}). Even if all of the tungsten atoms were contained in the core plasma, the present results overestimate the densities at least a factor of 3. Acutally, the present STRAHL simulation predicted much smaller densities by factors of 5 - 6. One may concern about uncertainty in the ionization balance. Since the present result was obtained as $n_W = n_{W27+}/n_{27}$, a larger fractional ion abundance of W^{27+}, n_{27}, would be able to reduce the result. However, recalling that the abundance ratio, n_{27}/n_{26}, is consistent with the present measurement, many times larger values of n_{27} are not plausible. Liu et al. [10] reported the same problem for total tungsten densities at $\rho = 0.7$ derived from EUV emission lines of W^{24+} around 3 nm at LHD. The tungsten density

calculated from the PEC using their CR model was roughly four times larger than that estimated from the pellet size, while the density calculated from the PEC using the ADAS code was considerably reduced. Generally, underestimation in PECs will cause overestimation in derived tungsten densities. So, the problem can be ascribed to underestimation of the PECs used for the ion density evaluation. The present PECs are obtained with the upper level populations including detailed atomic processes within the single ion, but omitting recombination and ionization from the adjacent charge states. Just recently Murakami et al. [32] reported that the EUV emission around 6 nm is enhanced by inclusion of the recombination processes and cascade from higher levels. Additional populations of the upper levels of the present M1 lines are also anticipated by such recombination from higher charge states and ionization from lower charge states, that is yet to be investigated.

5. Summary

In the present work, the visible M1 line emission of W^{27+} and W^{26+} was successfully observed at LHD by the pellet injection into the core plasmas under strong neutral beam heating. Radial ion density distributions of W^{27+} and W^{26+} were derived from the vertical profiles of the M1 line intensities on a horizontally elongated poloidal cross section and the calculated photon emission coefficients (PECs) using experimental electron temperature and density radial profiles. The transport-free ionization equilibrium model with ionization and recombination rate coefficients of ADAS database can explain approximately the ion abundance ratios of W^{27+} to W^{26+} in the core plasmas. The ion abundance ratios of the radial transport model implemented with STRAHL code agree with those of the transport-free model. Based on this result, the total tungsten density is derived from the W^{27+} ion density and its fraction ion abundance of the ionization equilibrium model.

After the tungsten injection, the central electron temperature decreases from 3 keV down to below 1 keV due to strong radiation of tungsten ions in the core. The radiation power is rpidly decreased in 400 ms, and it is followed by a stable phase with a tungsten content in the core. During the stable phase, the central electron temperature and the radial profile are almost constant, while the line-averaged electron density gradually increases due to a hydrogen gas puff. In this phase, the total tungsten densities in the core gradually decrease with time, while the densities at $\rho = 0.3$ do not change much leading to a hollow profile. After stopping the gas puff, onset of the reheat mode and significant increase of the core electron temperature were observed. The onset of the reheat mode apparently causes rapid decrease of the total tungsten density in the whole region, which coincides with decrease in the bolometric radiation power. This observation can be considered as the enhancement of the radial transport of tungsten during the reheat mode.

Significant overestimation of the tungsten densities derived from the visible M1 lines is found. This can probably be ascribed to inaccuracy remained in the present PECs calculated using the collisional-radiative model. The present PECs should be significantly underestimated due to omission of recombination and ionization from adjacent charge states.

And last but not least, since the primary heavy impurity of ITER would be tungsten, the visible forbidden lines of tungsten highly charged ions are also useful for plasma diagnostics, *e.g.* Doppler measurements of ion temperature [33] and plasma flow, because of their intrinsically narrow natural widths and less susceptibility to external fields.

Acknowledgements

The present work is supported by JSPS KAKENHI Grant Number 18H01201, the NIFS Collaboration Research program (NIFS20KLPF075, NIFS21KLPF083), and the NINS program of Promoting Research by Networking among Institutions (grant No. 01411702). The authors are grateful to the LHD Experiment Group for their excellent cooperation.

References

[1] PÜTTERICH, T., DUX, R., NEU, R., et al., Observations on the W-transport in the core plasma of JET and ASDEX Upgrade, Plasma Phys. Control. Fusion **55** (2013) 124036 (11pp).

[2] PÜTTERICH, T., DUX, R., BEURSKENS, M.N.A., et al., Tungsten screening and impurity control in JET, 24th IAEA FEC (8-13 Oct., 2012, San Diego, USA), EX/P3-15.

[3] LOARTE, A., REINKE, M.L., POLEVOI, A.R., et al., Tungsten impurity transport experiments in Alcator C-Mod to address high priority research and development for ITER, Phys. Plasmas **22** (2015) 056117 (15pp).

[4] YANG, X., MANAS, P., BOURDELLE, C., et al., Core tungsten transport in WEST long pulse L-mode plasmas, Nucl. Fusion **60** (2020) 086012 (14pp).

[5] PÜTTERICH, T., NEU, R., DUX, R., et al., Calculation and experimental test of the cooling factor of tungsten, Nucl. Fusion **50** (2010) 025012 (9pp).

[6] PÜTTERICH, T., FABLE, E., DUX, R., et al., Determination of the tolerable impurity concentrations in a fusion reactor using a consistent set of cooling factors, Nucl. Fusion **59** (2019) 056013 (28pp).

[7] PÜTTERICH, T., NEU, R., DUX, R., et al., Modelling of measured tungsten spectra for ASDEX Upgrade and predictions for ITER, Plasma Phys. Control. Fusion **50** (2008) 085016 (27pp).

[8] MURAKAMI, I., SAKAUE, H.A., SUZUKI, C., et al., Development of quantitative atomic modelling for tungsten

transport study using LHD plasma with tungsten pellet injection, Nucl. Fusion **55** (2015) 093016 (9pp).

[9] SUDO, S., TAMURA, N., SUZUKI, C., et al., Measurements of Radiation Power from High Z Impurities with TESPEL and Comparison with Theoretical Calculations, Plasma Fusion Res. **9** (2014) 1202147 (3pp).

[10] LIU, Y., MORITA, S., MURAKAMI, I., et al., Density evaluation of tungsten W^{24+}, W^{25+}, and W^{26+} ions using unresolved transition array at 27-34 Å in Large Helical Device, Jpn. J. Appl. Phys. **57** (2018) 106101 (9pp).

[11] KATO, D., GOTO, M., MORITA, S., et al., Observation of visible forbidden lines from highly charged tungsten ions at the large helical device, Phys. Scr. T**156** (2013) 014081 (3pp).

[12] KATO, D., SAKAUE, H.A., MURAKAMI, I., et al., Observation of visible forbidden lines of tungsten highly charged ions in LHD core plasmas and its application to ion distribution analysis, 26th IAEA FEC (17-22 Oct., 2016, Kyoto, Japan), EX/P8-14.

[13] ISOBE, M., NAGAOKA, K., YOSHIMURA, Y., et al., Reheat Mode Discharges in Search of Attainable High Stored Energy and Density Limit of Compact Helical System, Fusion Science and Technology **50** (2006) 229-235.

[14] HUANG, X.L., MORITA, S., OISHI, T., et al., Coaxial pellets for metallic impurity injection on the large helical device, Rev. Sci. Instrum. **85** (2014) 11E818 (4pp).

[15] ZHOU, H.Y., MORITA, S., GOTO, M., and DONG, C.F., Zeff profile diagnostics using visible bremsstrahlung continuum for nonaxisymmetric plasmas with finite β in large helical device, J. Appl. Phys. **107** (2010) 053306 (11pp).

[16] FEI, Z., LI, W., GRUMER, J., et al., Forbidden-line spectroscopy of the ground-state configuration of Cd-like W, Phys. Rev. A **90** (2014) 052517 (6pp).

[17] FEI, Z., ZHAO, R., SHI, Z., et al., Experimental and theoretical study of the ground-state M1 transition in Ag-like tungsten, Phys. Rev. A **86** (2012) 062501 (5pp).

[18] KOMATSU, A., SAKODA, J., NAKAMURA, N., et al., Visible spectroscopy of highly charged tungsten ions, Phys. Scr. T**144** (2011) 014012 (3pp).

[19] WATANABE, H., NAKAMURA, N., KATO, D., et al., Lines from highly charged tungsten ions observed in the visible region between 340 and 400 nm, Can. J. Phys. **90** (2012) 497–501.

[20] QUI, M.L., ZHAO, R.F., GUO, X.L., et al., Investigation of transitions between metastable levels of the first excited configuration of palladium-like tungsten, J. Phys. B: At. Mol. Opt. Phys. **47** (2014) 175002 (8pp).

[21] SAFRONOVA, U.I. and SAFRONOVA, A.S., Wavelengths and transition rates for nl–n'l' transitions in Be-, B-, Mg-, Al-, Ca-, Zn-, Ag- and Yb-like tungsten ions, J. Phys. B: At. Mol. Opt. Phys. **43** (2010) 074026 (15pp).

[22] DING, X.B., KOIKE, F., MURAKAMI, I., et al., Ab initio multi-configuration Dirac–Fock calculation of M1 visible transitions among the ground state multiplets of the W^{26+} ion, J. Phys. B: At. Mol. Opt. Phys. **44** (2011) 145004 (6pp).

[23] BAR-SHALOM, A., KLAPISCH, M., OREG, J., HULLAC, and integrated computer package for atomic processes in plasmas, JQSRT **71** (2001) 169-188.

[24] GU, M.F., The flexible atomic code, Can. J. Phys. **86** (2008) 75-689.

[25] JÖNSSON, P., HE, X., FROESE FISCHER, C., The grasp2K relativistic atomic structure package, Comput. Phys. Commun. **177** (2007) 597-622.

[26] HINNOV, E. and MATTIOLI, M., Observations of multiply ionized tungsten radiation in the PLT discharges, Phys. Lett. A **66** (1978) 109-111.

[27] ASMUSSEN, K., FOURNIER, K.B., LAMING, J.M., et al., Spectroscopic investigations of tungsten in the EUV region and the determination of its concentration in tokamaks. Nucl. Fusion **38** (1998) 967.

[28] HARTE, C.S., SUZUKI, C., KATO, T., et al., Tungsten spectra recorded at the LHD and comparison with calculations, J. Phys. B: At. Mol. Opt. Phys. **43** (2010) 205004.

[29] RADTKE, R., BIEDERMANN, C., SCHWOB, J.L., et al., Line and band emission from tungsten ions with charge 21+ to 45+ in the 45 – 70 Å range, Phys. Rev. A **64** (2001) 012720.

[30] OPEN-ADAS, https://open.adas.ac.uk/

[31] BERHINGER, K., Description of the impurity transport code STRAHL, JET-R(87)08 (1987), JET Joint Undertaking, Culham; DUX, R., *Technical Report No* 10/30 (2006), IPP, Garching, Germany.

[32] MURAKAMI, I., KATO, D., OISHI, T., et al., Progress of tungsten spectral modeling for ITER edge plasma diagnostics based on tungsten spectroscopy in LHD, Nuclear Materials and Energy **26** (2021) 100923 (10pp).

[33] FUJII, K., TAKAHASHI, Y., NAKAI, Y., et al., Visible emission spectroscopy of highly charged tungsten ions in LHD: II. Evaluation of tungsten ion temperature, Phys. Scr. **90** (2015) 125403.

Table 1 Wavelengths (nm) of five M1 lines of W^{q+} in 330 – 390 nm observed at LHD. Numbers in parentheses represent uncertainty in the last digits. Existing measurements by electron-beam-ion-traps are shown in the column EBIT. Theoretical wavelengths calculated by the relativistic many-body perturbation theory and the multiconfiguration Dirac-Hartree-Fock method are shown in the columns of RMBPT and MCDHF, respectively.

q	LHD	EBIT	RMBPT	MCDHF	Transition
26	333.70(2)	333.748(9)[1]*	333.2[1]	334.4[1]	$(4f^2)\ ^3F_4 \rightarrow\ ^3F_3$
	335.73(2)	335.758(11)[1]*	333.6[1]	334.5[1]	$(4f^2)\ ^3F_4 \rightarrow\ ^1G_4$
	389.39(2)	389.433(12)[1]*, 389.41(6)[2], 389.35(3)[3]	-	388.43[7]	$(4f^2)\ ^3H_5 \rightarrow\ ^3H_4$
27	337.73(2)	337.743(26)[4]	338.4[6]	338.18[4]	$(4f)\ ^2F_{7/2} \rightarrow\ ^2F_{5/2}$
28	344.48(2)	344.489(33)[5]	345.87[5]	-	$(4d^9 4f)\ (5/2,7/2)_4 \rightarrow (5/2,5/2)_3$

(1) Fei et al. (2014) [15], (2) Komatsu et al. (2011) [17], (3) Watanabe et al. (2012) [18], (4) Fei et al. (2012) [16], (5) Qui et al. (2014) [19], (6) Safronova (2010) [20], (7) Ding et al. (2011) [21].

*Converted to wavelength in vacuum.

Table 2 Theoretical transition rates (s^{-1}) of the M1 lines. HULLAC results are used for the present calculations.

q	Transition	HULLAC	FAC	GRASP2K
26	$(4f^2)\ ^3F_4 \rightarrow\ ^3F_3$	281	273	294
	$(4f^2)\ ^3F_4 \rightarrow\ ^1G_4$	241	234	254
27	$(4f)\ ^2F_{7/2} \rightarrow\ ^2F_{5/2}$	291	-	285.8

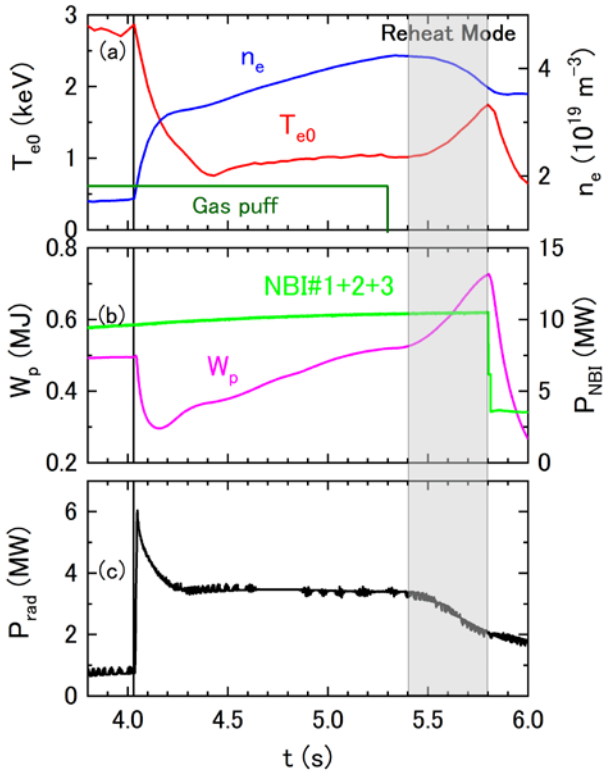

figure 1 Time traces of (a) the central electron temperature, T_{e0}, and the line-averaged electron density, n_e, (b) the plasma stored energy, W_p, and the NBI port-through power, P_{NBI}, and (c) the total radiated power, P_{rad}. A tungsten pellet is injected at t = 4.03 s. Shot number is 121534.

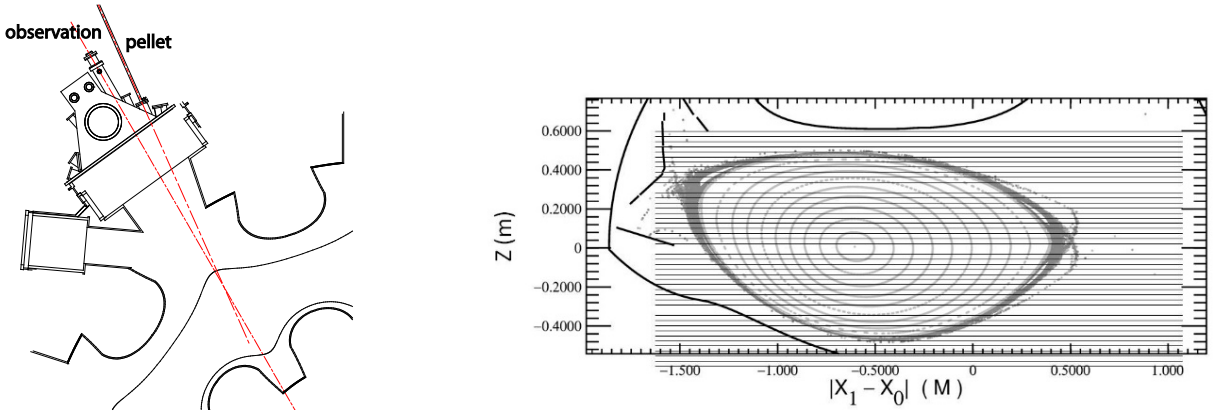

figure 2 Left) A top view of the observation and pellet injection ports. Right) Horizontally elongated poloidal cross section and lines of sight viewing from the right-hand side. [15]

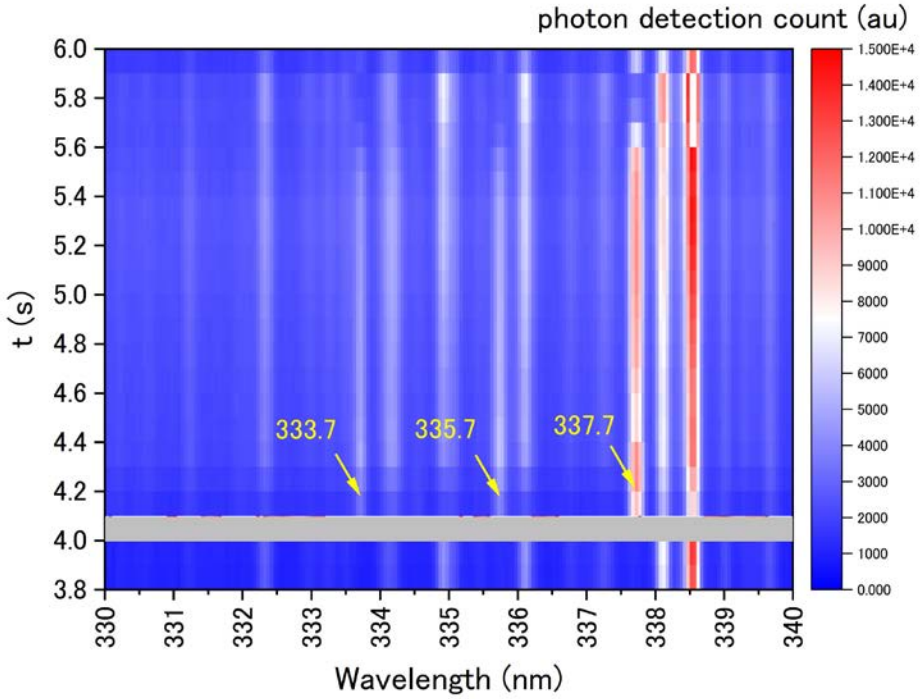

figure 3 Time trace of photon detection counts. The grey hatched area represents emission zone of pellet ablation cloud. Three lines indicated by yellow arrows are the M1 lines: W^{26+} ($4f^2$) $^3F_4 \rightarrow {}^3F_3$ at 333.7 nm and $^3F_4 \rightarrow {}^1G_4$ at 335.7 nm, and W^{27+} (4f) $^2F_{7/2} \rightarrow {}^2F_{5/2}$ at 337.7 nm.

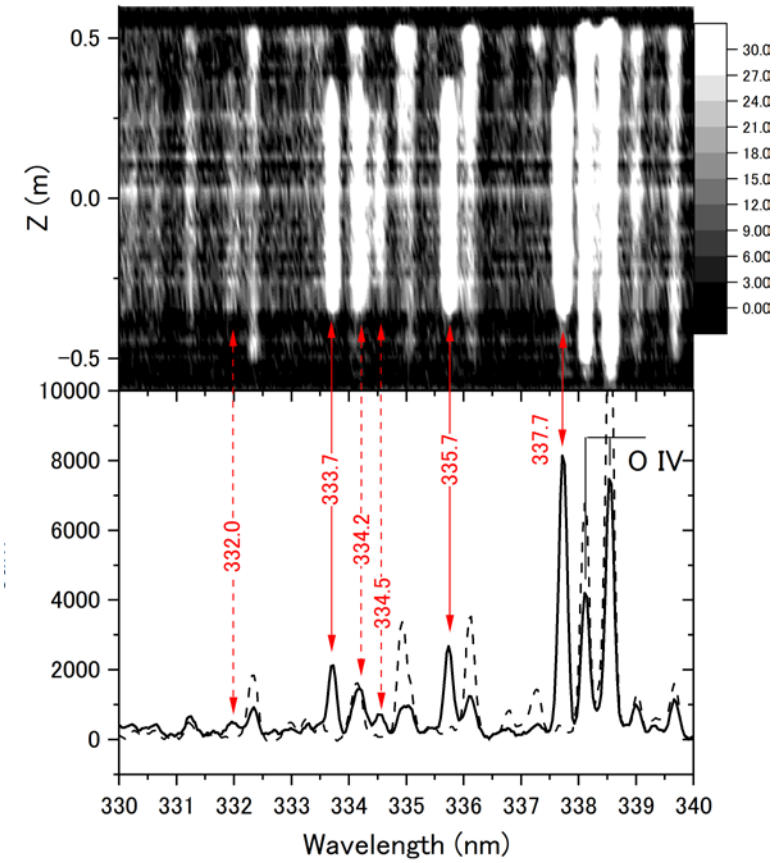

figure 4 Line emission spectra in 330 - 340 nm for t = 4.1 – 4.138 s. The dashed black line stands for the spectrum before the tungsten injection. Upper panels show vertical profiles of line-integrated intensities. Red arrows indicate the emission lines assigned to tungsten. Numbers are the central wavelengths in nm.

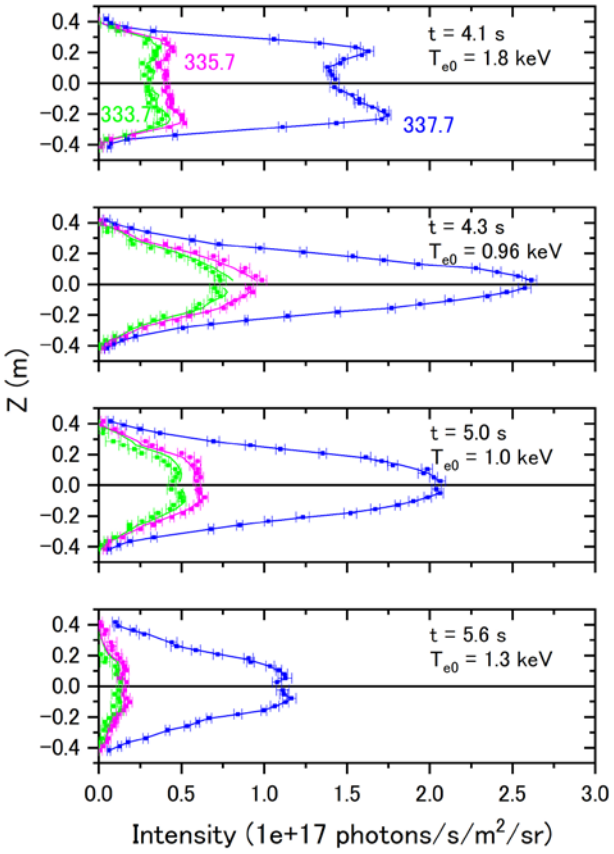

figure 5 Absolute line-integrated intensity of M1 lines at t = 4.1, 4.3, 5.0, and 5.6 s. Note that each measurement took the exposure time of 38 ms. Blue color is for the M1 line of W^{27+} at 337.7 nm, pink and green color for the M1 lines of W^{26+} at 335.7 nm and 333.7 nm, respectively. T_{e0} are corresponding central electron temperatures averaged in the exposure time.

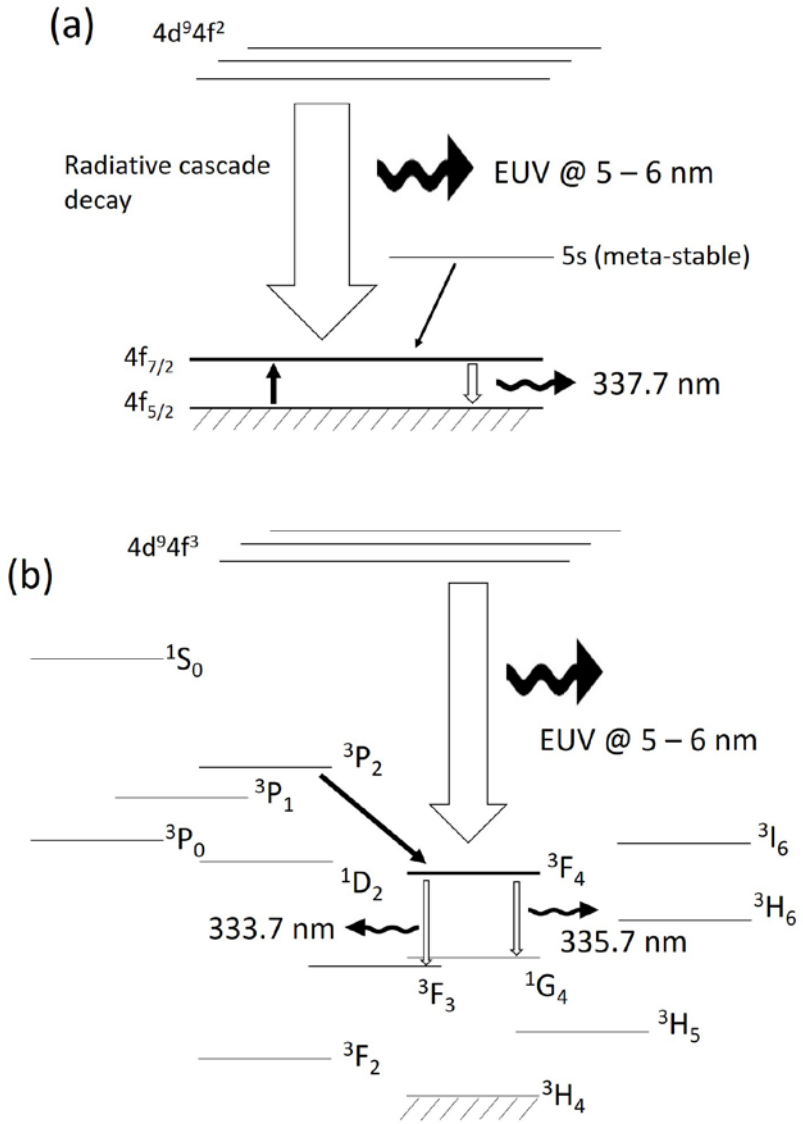

figure 6 Schematic diagrams of M1 line emission for (a) W^{27+} (4f) and (b) W^{26+} ($4f^2$). Solid and open arrows indicate population flows to the upper levels via collisional transition and radiative decay, respectively. Widths of the arrows represent magnitudes of the flow rates in the steady state.

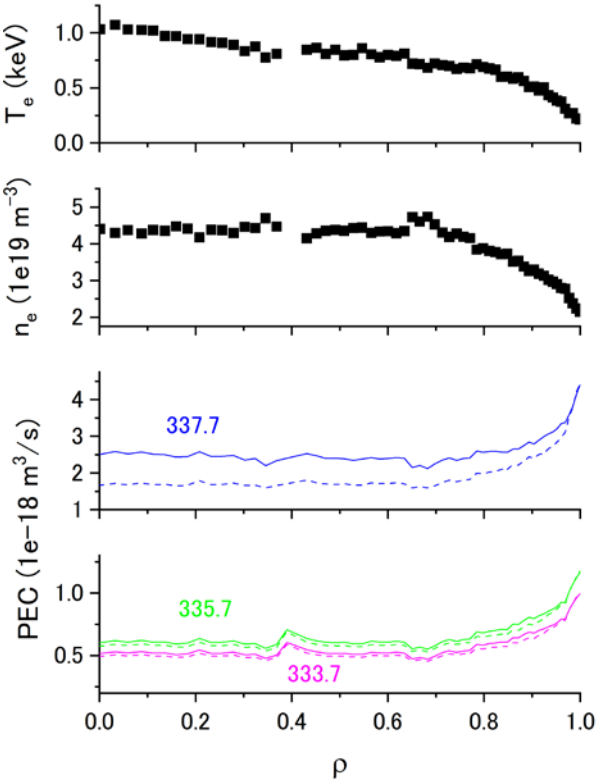

figure 7 Local electron temperatures (T_e) and densities (n_e) measured by Thomson scattering as a function of the normalized minor radius ρ for t = 5.0 s of the present discharge, and corresponding photon emission coefficients (PECs) of three M1 lines (solid lines). Dashed lines are the PECs without proton collision effects. Numbers are wavelengths (nm) of the M1 lines.

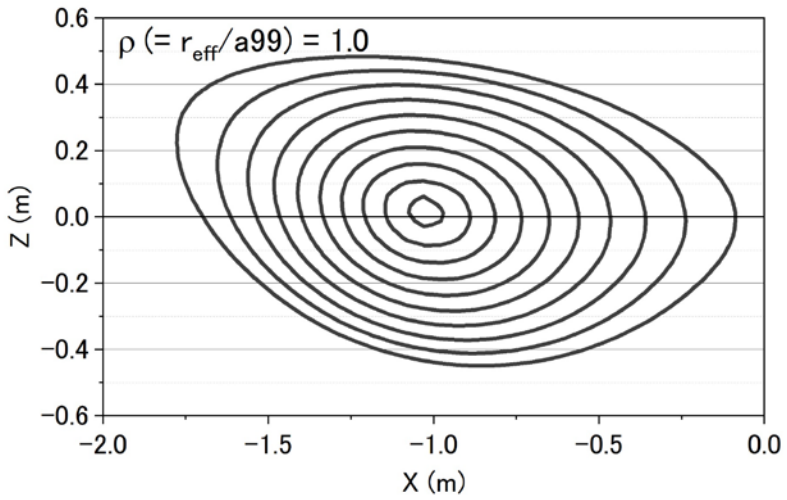

figure 8 Geometry of a poloidal cross section, and a contour plot of the normalized minor radius $\rho \leq 1$ incrementing by 0.1.

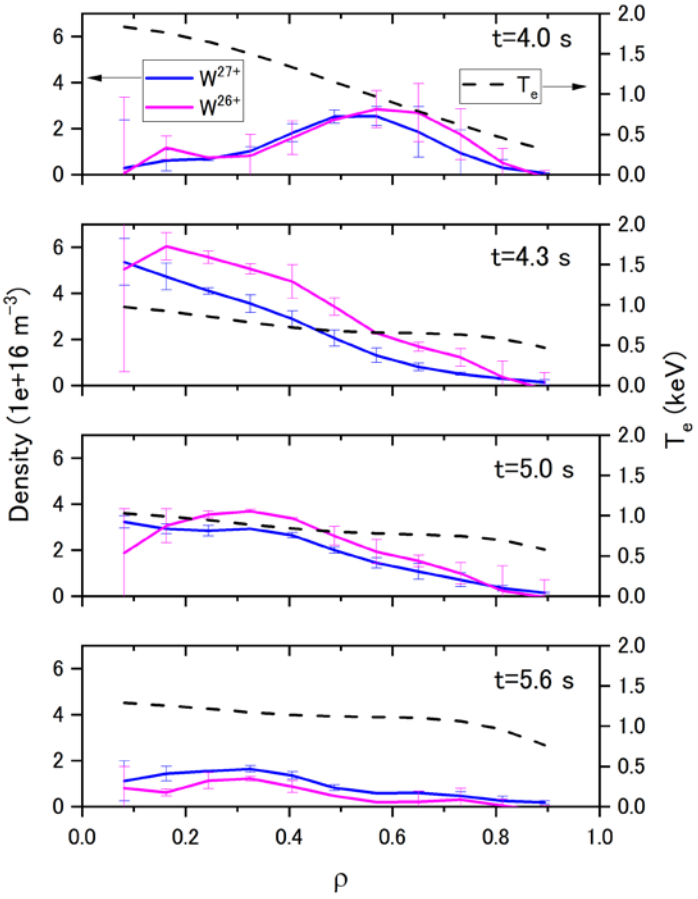

figure 9 Radial distributions of W^{26+} (pink) and W^{27+} (blue) densities, and corresponding electron temperature profiles (dashed curves).

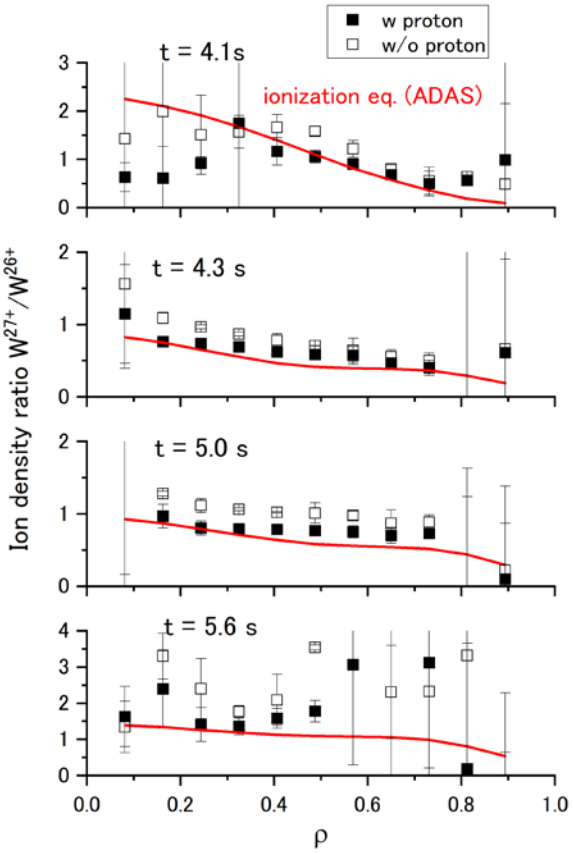

figure 10 Ion density ratios of W^{27+} to W^{26+} as a function of ρ with (solid) and without (open) proton collision effects. Red curves are the ratios of a transport-less ionization equilibrium model. The ionization equilibrium density ratios were calculated using CR ionization (scd50_w) and recombination rate coefficients (acd50_w) of ADAS database [29].

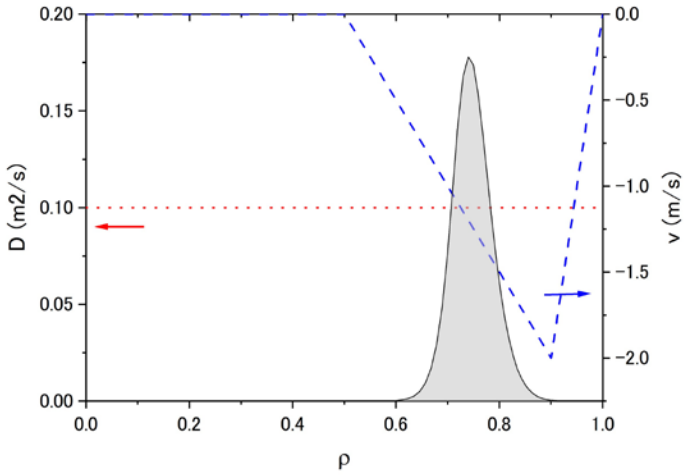

figure 11 Transport coefficients used in the present STRAHL simulation. The red dotted line stands for a uniform diffusion coefficient and the blue dashed line for the inward convection velocity. 6.8×10^{17} neutral W are deposited in the region indicated by grey.

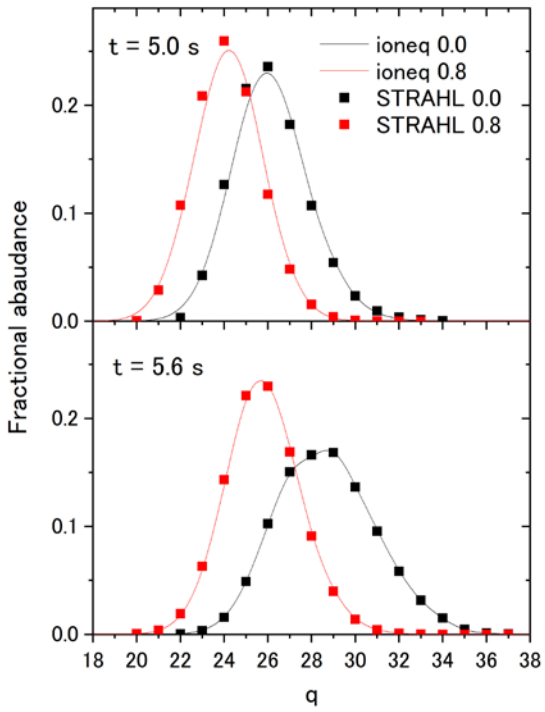

figure 12 Fractional ion abundance of W^{q+}. Black squares stand for the ion abundance at the centre $\rho = 0$ and red squares for at the edge $\rho = 0.8$ obtained by the present transport simulation. Solid curves represent the ion abundance of the transport-free ionization equilibrium model.

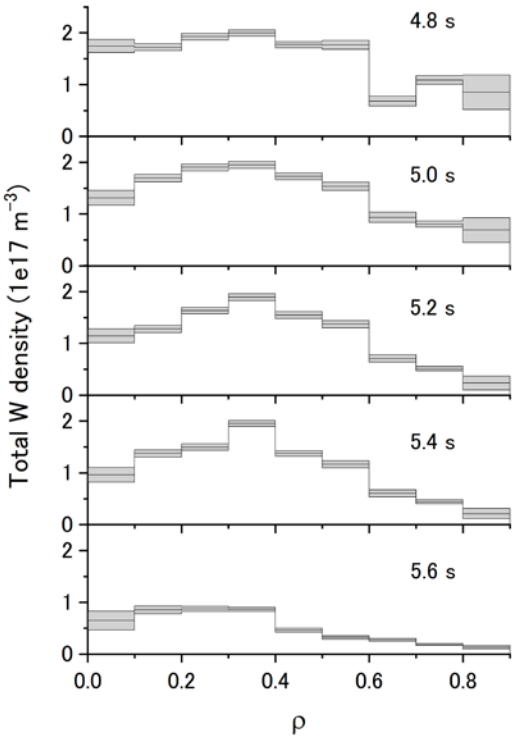

figure 13 Evolution of the total W density in the core. Gray zones represent uncertainty (1σ).

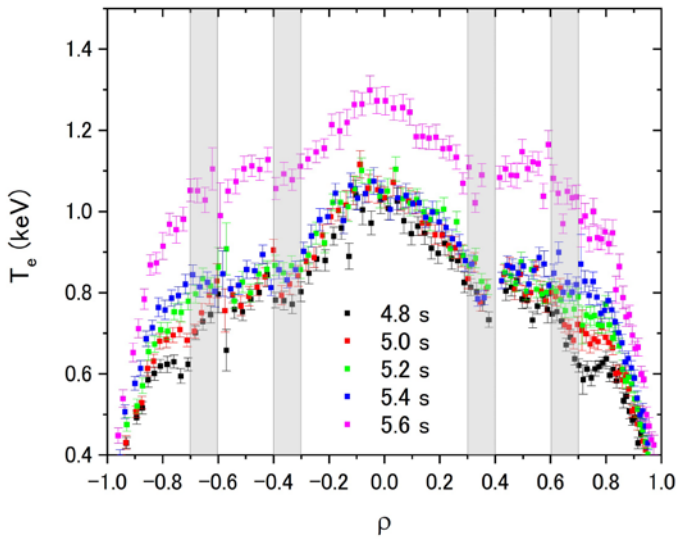

figure 14 Evolution of electron temperature profiles measured by Thomson scattering.